

# Direct control of high magnetic fields for cold atom experiments based on NV centers

Alexander Hesse,<sup>1</sup> Kerim Köster,<sup>1</sup> Jakob Steiner,<sup>2,3</sup> Julia Michl,<sup>2</sup> Vadim Vorobyov,<sup>2</sup> Durga Dasari,<sup>2</sup> Jörg Wrachtrup,<sup>2,4</sup> and Fred Jendrzejewski<sup>1</sup>

<sup>1</sup>*Kirchhoff-Institut für Physik, Im Neuenheimer Feld 227, 69120 Heidelberg*

<sup>2,3</sup>*Physikalisches Institut, Center for Applied Quantum Technologies, IQST, Pfaffenwaldring 57, 70569 Stuttgart*

<sup>3</sup>*Paul-Scherrer-Institute, 5323 Villigen, Switzerland*

<sup>4</sup>*Max Planck Institute for Solid State Research, Heisenbergstraße 1, 70569 Stuttgart, Germany*

(Dated: November 9, 2020)

In cold atomic gases the interactions between the atoms are directly controllable through external magnetic fields. The magnetic field control is typically performed indirectly by stabilizing the current through a pair of Helmholtz coils, which produce this large bias field. Here, we overcome the limitations of such an indirect control through a direct feedback scheme, which is based on nitrogen-vacancy centers acting as a magnetic field sensor. This allows us to measure and stabilize fields of 4.66 mT down to 12 nT RMS noise over the course of 24 h, measured on a 1 Hz bandwidth. We achieve a control of better than 1 ppm after 20 minutes of integration time, ensuring high long-term stability for experiments. This approach extends direct magnetic field control to strong magnetic fields, which could enable new precise quantum simulations in this regime.

## I. INTRODUCTION

The direct control of modest magnetic fields up to 1 mT enabled experiments with cold atoms on diverse topics, like spin squeezing close to a Feshbach resonance [1, 2], the quantum simulation of scaling dynamics far from equilibrium [3] or of a scalable building block for lattice gauge theories in atomic mixtures [4]. In all these cases, the direct magnetic field control is based on active feedback from a fluxgate sensor, which limits this class of experiments to magnetic fields below 1 mT, the working range of fluxgate sensors [5]. Many phenomena, like droplet formation close to a heteronuclear Feshbach resonance [6] or spin changing collisions between fermionic and bosonic species [7], do however occur at much higher field strengths, reaching up to a few tens of mT. Direct magnetic field control has so far not been possible in this regime due to a lack of suitable sensors, making precision experiments challenging.

This shows the need for alternative sensors able to measure large magnetic fields with high precision. Over the last years, several sensors based on quantum systems with the potential to close this gap have been tested, summarized in Table I. Most prominently, SQUIDs can measure magnetic fields with sensitivities in the  $\text{fT}/\sqrt{\text{Hz}}$  regime [8, 9], with atomic gases reaching comparable or slightly better sensitivities at low fields [10–13]. However, the large size of these systems as well as the demanding setup required for probing them makes them impractical as a sensor for an active magnetic field stabilization.

The nitrogen-vacancy (NV) center in diamond provides a versatile and compact magnetic field sensor, covering ranges up to several tens of T with precisions below  $1 \text{ pT}/\sqrt{\text{Hz}}$  [14] for AC magnetic fields. For measurements which approach the DC regime, sensitivities of a few  $10 \text{ pT}/\sqrt{\text{Hz}}$  and below have been reported [15–18]. Due to their small size, they are the perfect candidate for magnetic field stabilizations [19, 20] past the range of fluxgate

sensors, and allow the study of spin dynamics in regimes previously not experimentally accessible.

In this article, we investigate the direct control of homogeneous magnetic fields based on such NV centers. Our experimental setup is sketched in Fig. 1. A set of Helmholtz coils produces a homogeneous magnetic field  $B_0$ , which is directly proportional to the applied control current flowing through the coils. The magnetic field is sensed through the fluorescence of a compact NV center magnetometer. In the magnetometer, we measure the optically detected magnetic-resonance features (ODMR) by dressing the ground state spin triplet with a microwave signal of frequency  $\nu$ . A dip appears in the fluorescence intensity  $I$  of the NV centers when  $\nu$  coincides with one of the Zeeman shifted transition frequencies within the triplet [21]. The derivative  $S = dI/d\nu$  is then used as an error signal for the feedback loop. The magnetic field strength has been monitored through a second, independent NV magnetometer over the course of 24 hours. We achieved a magnetic field stability of  $\sigma_{DC} = 12 \text{ nT}$  measured over a 1 Hz bandwidth, while shorter measurements over the full control loop bandwidth of 1 kHz yielded magnetic field noise of 126 nT. Replacing this second diamond with the cold atomic clouds of interest in the future will allow regulating the magnetic field the atoms experience.

The remainder of the paper is structured as follows: In section II we review the employed detection of the magnetic field and how we separate thermal drifts from magnetic field changes. In section III we discuss the control of the magnetic field and benchmark our system in a detailed fashion. We end with an outlook for more compact solutions beyond this proof-of-concept in section IV.

## II. MAGNETOMETRY METHOD

For generating the magnetic field signal on both our sensors we employ an ODMR scheme [31], which we sum-

Sensor	Maximum operation field, mT	Sensitivity, $\text{nT}/\sqrt{\text{Hz}}$	Blocked optical access, mm	References
Hall sensor	70 – 200	100 – 500	1.5 – 3	[22–24]
Fluxgate	1	$5 \cdot 10^{-3} - 10^{-2}$	20 – 30	[5, 25, 26]
Giant magnetoeimpedance	$250 \cdot 10^{-3} - 1$	$10^{-3} - 10^{-2}$	0.1 – 20 <sup>a</sup>	[25, 26]
Atomic vapor cell	$10^{-1}$	$10^{-7} - 10^{-1}$	2 – 20	[10–12]
SQUID	$10^4$	$10^{-6} - 10^{-2}$	$10^{-1} - 20$ <sup>b</sup>	[25, 27–29]
<b>NV center</b>	<b><math>10^4</math></b>	<b><math>9 \cdot 10^{-4} - 10</math></b>	<b><math>10^{-1} - 2</math></b>	[15–18, 30]

<sup>a</sup> Based on the orientation of the wire

<sup>b</sup> Requires cryogenic cooling

TABLE I. Comparison of commercially available Hall- and Fluxgate sensors with GMI magnetometers, atomic vapor cells, SQUIDS and NV centers. The extent of the sensor head is used to quantify the optical access to the experiment blocked.

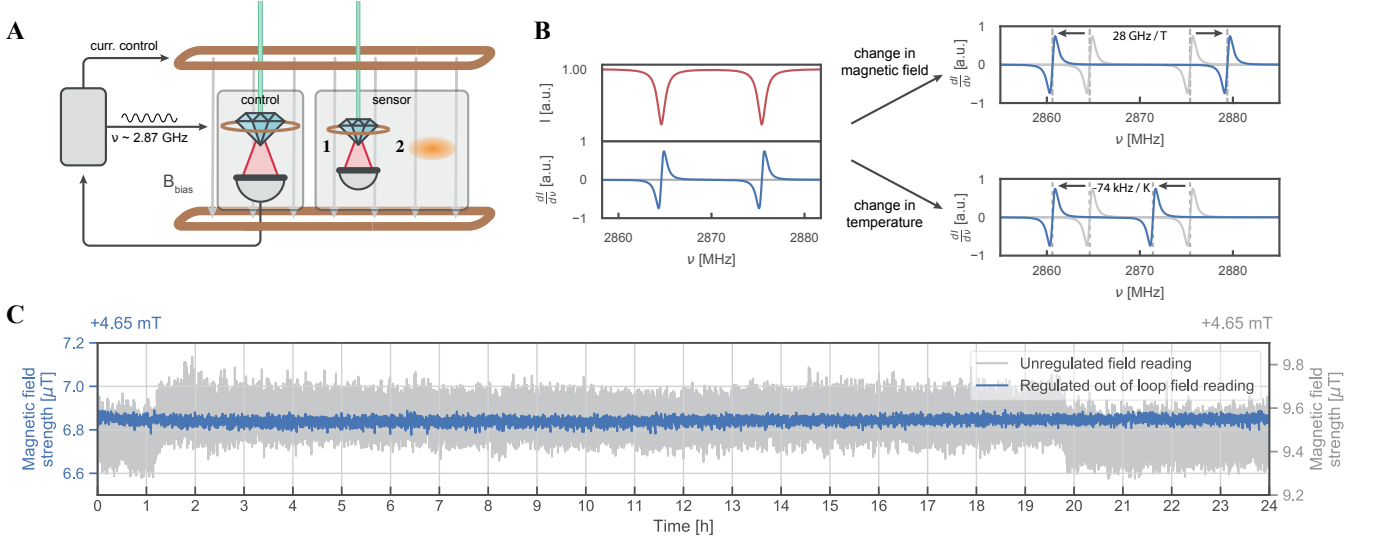


FIG. 1. (A) Basic experimental setup: The NV centers are positioned in a magnetic field generated by a pair of Helmholtz coils. They are excited by a green laser, and their red fluorescence is collected on a photodiode. This signal is fed into a control circuit, which also generates the microwave signal applied to the NV centers via a wire loop. From the fluorescence a magnetic field reading is extracted, and used to regulate the current through a second, low inductance coil pair. (1) The quality of the magnetic field stabilization is monitored on a second, independent setup placed close to the first sample. (2) In the future, this second NV sensor will be replaced by the cold quantum gas used in our experiments, such that it experiences stable magnetic fields. (B) Shift of the two transitions  $m_s = 0 \rightarrow m_s = -1$  and  $m_s = 0 \rightarrow m_s = 1$  with temperature and magnetic field, as visible in the fluorescence signal. Using a lock-in scheme we extract the derivative of the spectrum. (C) 24 h measurements comparing the unregulated and regulated magnetic field measured by the out of loop sensor. In the regulated case (blue curve), the signal of the NV control is used to actively stabilize the magnetic field. In the unregulated case (grey curve) the magnetic field is just set by the current output of the power supply. In addition to higher overall noise for the current stabilized field, jumps in the field strength created by other experiments nearby are visible here.

marize in Fig. 2. The NV center has a spin  $S = 1$  in its ground state. It is optically pumped by a green laser, and consequently emits fluorescence above 637 nm. The unsplit  $m_s = \pm 1$  states lie  $D \approx 2.87 \text{ GHz}$  (also called the zero field splitting (ZFS)) above the  $m_s = 0$  state and hence can be coupled to the ground state through standard microwave techniques (see appendix B). At nonzero magnetic field, the  $m_s = \pm 1$  states experience a Zeeman shift of approximately  $\pm h\gamma_e \vec{B}_0 \cdot \hat{n}$ , where  $B_0$  is the magnetic field strength,  $\gamma_e = 28 \text{ GHz/T}$  is the gyromagnetic ratio of the electron, and  $\hat{n}$  is the projection of the magnetic field onto the NV center axis. For the  $m_s = \pm 1$

states a nonradiative decay channel to the ground state leads to a slight decrease in fluorescence, allowing us to extract the transition frequencies  $\nu_{+1}$  and  $\nu_{-1}$  from the fluorescence spectrum.

We use a lock-in scheme by frequency modulating the microwave signals applied at modulation frequencies  $\omega_{\text{mod} \pm 1}$  of a few tens of kHz to generate the error signals  $S_{-1} = \frac{dI}{d\nu}|_{\nu=\nu_{-1}}$  and  $S_{+1} = \frac{dI}{d\nu}|_{\nu=\nu_{+1}}$  at both transitions. The information gained by monitoring both transitions can then be used to compensate for temperature fluctuations of the sample (see appendix C), which would shift both resonance frequencies in the same direction, as il-

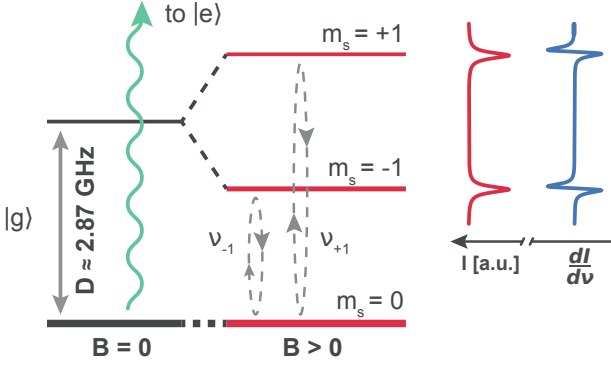


FIG. 2. Simplified  $\text{NV}^-$  center level scheme: The internal spin state can be read out by transferring the system into the excited state - if the centers were in the  $m_s = \pm 1$ , the fluorescence will not be as bright (as indicated by the width of the red lines). Now the Zeeman shift of the  $m_s = \pm 1$  levels can be measured by finding the fluorescence minima. By modulating the microwave frequencies  $\nu_{-1}$  and  $\nu_{+1}$ , a lock-in scheme can be employed.

lustrated in Fig. 1 B [32].

The frequency modulated signal necessary for this scheme is generated on a StemLab RedPitaya, and mixed with the two channels of a microwave generator to shift them to the microwave regime to address the two transitions. After that, they are amplified and applied to a wire loop placed around the diamond sample.

The diamond samples used were grown with the HPHT technique, have a natural abundance of  $^{13}\text{C}$  and are type 1b diamonds with a natural linewidth of 1.3(1) MHz, heatsunk to a sapphire window. The samples are placed in a homogeneous magnetic field generated by a pair of Helmholtz coils, with a second pair of coils with only few windings wound onto in order to regulate the magnetic field over a high bandwidth (see appendix D for further details).

The fluorescence of our sample is collected efficiently by a compound parabolic concentrator [33], and the remaining excitation light is filtered out by a longpass filter (see appendix A for more details). It is measured using an auto-balanced photodetector [34, 35], whose output is also digitized by the RedPitaya. A modified version of PyRPL [36] is used to process the data on its FPGA, generating an error signal at both transitions to regulate the current through the low inductance coil pair.

The position of these transitions depends on the magnetic field, but also on other factors, most importantly temperature. This effect shifts both transitions equally. As the magnetic field shift both lines in opposite directions, we only used the difference signal  $\Delta S = S_{+1} - S_{-1}$  as a control for the magnetic field. The sum of the two error signals  $\bar{S} = S_{+1} + S_{-1}$  is directly proportional to the shift of the ZFS  $D$  and the off-axis magnetic field.

The spectrum of the signals obtained this way are shown in Fig. 3: One can see that the noise at 50 Hz and harmonics, which is magnetic field noise created by

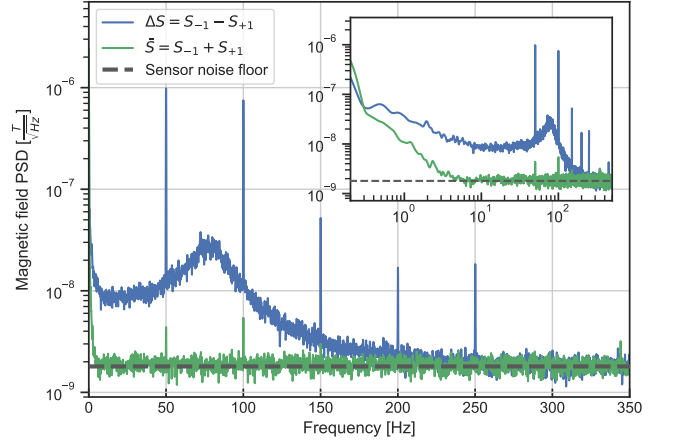


FIG. 3. Sum and difference of the error signals obtained on the two transitions. The inset shows the same data plotted on a logarithmic frequency axis, indicating that the temperature noise starts to dominate at low frequencies. The dashed grey line indicates the sensor noise floor  $\sigma_s$ .

the power line, is by a factor 200 smaller in  $\bar{S}$  compared to  $\Delta S$ . From this we conclude that we separate in-axis reading well from off-axis magnetic field and temperature readings, which helps us to stabilize the field in the axis of interest without introducing noise into the system. In the inset we present the same data on a logarithmic frequency scale. Here one can clearly identify the strong temperature noise, which would eventually become dominant at low frequencies in the individual error signals  $S_{+1}$  and  $S_{-1}$ .

In total, we collect about 3.4 mW of fluorescence on the signal photodiode for both sensors, leading to a photocurrent of 1.7 mA. This allows us to calculate the shot noise on the photocurrent using  $\sigma_{I,SN} = \sqrt{2 \cdot I \cdot e \cdot \Delta f}$  [16]. In this equation,  $I$  denotes the photocurrent,  $e$  the elementary charge, and  $\Delta f$  is the single-sided measurement bandwidth.

The photocurrent shot noise can be converted to the shot noise limited magnetic field sensitivity  $\sigma_{B,SN} = \sigma_{I,SN} \cdot dB/dI$  by multiplying it with the inverse of the lock-in slope. This yields a shot noise limited noise floor of  $\sigma_{B,SN} \approx 0.97 \text{ nT}/\sqrt{\text{Hz}}$  for the magnetic field signal, whereas we observe a total noise floor of  $\sigma_S \approx 1.8 \text{ nT}/\sqrt{\text{Hz}}$  experimentally. The main additional contributions to this noise floor are not entirely cancelled fluorescence intensity noise as well as microwave noise, with a smaller contribution stemming from the shot noise on the reference photocurrent, which was not considered here.

### III. MAGNETIC FIELD STABILIZATION

After the characterization of the magnetic field sensors, we employ them to monitor the magnetic field noise and actively stabilize it. The time trace of these measurements over 24 h was presented in Fig. 1 C. In Fig. 4 A we

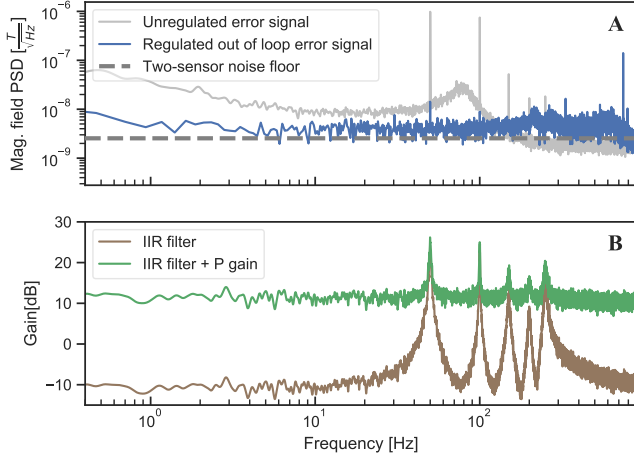


FIG. 4. **(A)**: Magnetic field error signal for an open feedback loop (in grey) and for a closed feedback loop, measured on an independent sensor (in blue). **(B)**: The total feedback gain consists of a PI signal (the I part not shown) as well as a IIR filter to increase the noise suppression at 50 Hz and harmonics.

investigate the associated spectrum at high frequencies. In the open loop configuration (grey curve in the figures), the magnetic field is set to  $B_0 = 4.67$  mT by applying a current of  $\approx 6.3$  A to a pair of Helmholtz coils. The noise spectrum in Fig. 4 A reveals that the power supply driving this current introduces magnetic field noise of a few  $10$  nT/ $\sqrt{Hz}$  up to a frequency of 200 Hz. Above this cut-off frequency, which is set by the inductance of the coils, the detected magnetic field noise is again limited by the sensor noise.

We use the error signal of the magnetometer to actively stabilize the magnetic field through a feedback system and sense the resulting magnetic field on the independent sensor. The feedback is created by feeding the error signal into a PI controller (which is realized on the RedPi-taya's FPGA) that regulates the current through the low inductance coil pair. Because particularly strong magnetic field noise is present at 50 Hz and harmonics due to power line noise, we implement an IIR filter to increase the feedback loop gain at those frequencies as shown in Fig. 4 B.

We monitor the resulting magnetic field over 24 h as shown by the blue curve in Fig. 1 C. Over a bandwidth of 1 Hz we reduce the magnetic field noise of 65 nT down to  $\sigma_{DC} = 12$  nT. The DC component of the stability is essential for the repeatability of the quantum simulation experiments, where single runs are typically performed on the timescale of up to a minute and datasets are accumulated over the duration of days [37, 38]. The spectrum of a short-term measurement covering the full stabilization bandwidth is shown in Fig. 4 A: Here we see, that up to the control loop's bandwidth of 1 kHz magnetic field noise is reduced down to  $\sigma_{AC} = 126$  nT. Within the noise spectrum, peaks that might coincide with a mo-

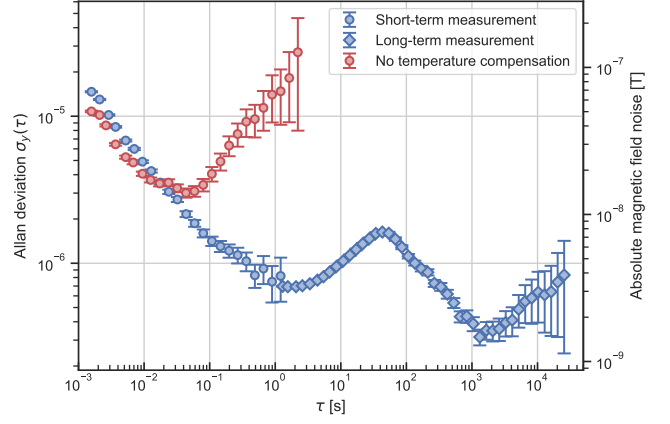


FIG. 5. Allan deviation of the stabilized magnetic field. The blue diamonds are obtained from the long term measurement that is visualized in Fig. 1 C. It is complemented by a set of short term measurements (blue circles) with duration of 4 s and a resolution of 0.2 ms that connect directly to the long term measurements at a time scale of 1 s. For up to a few seconds the Allan deviation decreases with  $1/\sqrt{\tau}$  as expected for white noise on the error signal. A noise peak at  $\tau = 60$  s can be observed, which results from the retuning routine for the microwave generators. The red curve shows the Allan deviation obtained when the magnetic field is only locked to  $S_{-1}$ , so without any additional temperature noise cancellation. Its increase after approximately 100 ms is due to uncompensated temperature fluctuations, which are strongly suppressed in the full scheme.

tional resonance are especially problematic. This makes the reduction of the 50 Hz noise by a factor of about 70 a potentially crucial improvement for the fidelity of the quantum simulator.

From these two measurements we calculate the Allan deviation of the magnetic field stability, as shown in Fig. 5. Additionally, a short-term measurement only stabilized to  $S_{-1}$ , so without our temperature noise compensation scheme, is shown, clearly indicating the necessity of this scheme. The short-term measurement with temperature noise compensation drops with the  $\tau^{-1/2}$  scaling expected from white frequency noise. The long-term measurements directly connects to the short-term measurement at the integration time of 1 s. For longer integration times we observe a broad peak centered at 60 s. This is due to the dead time during the retuning of the microwave sources once a minute to follow the temperature shifts of the NV center's transitions (see appendix C). We also attribute the slight increase in magnetic field noise at low frequencies in Fig. 4 A to these retuning effects. We hence see them as the main source of the low frequency noise  $\sigma_{DC}$ .

Our work extends previous work on feedback control using NV centers: In the work of [20], feedback from the electron spin of NV centers was used to stabilize the precession of the  $^{14}\text{N}$  nuclear spin ensemble associated with them by regulating the detuning of a Ramsey se-

quence. This allowed to reach longterm stabilities of several hours. Similarly, in [39], a feedback loop tracks resonance pairs of NV centers by supplying feedback to the microwave frequency. This technique offered an increase in dynamic range, and made it robust against temperature fluctuations. In [19] a second NV magnetometer, which was operated close to the sample of the NV-NMR setup, was utilised to stabilize the external magnetic field. The short-term stabilization of up to 5 minutes showed a magnetic field stability of  $\sigma_B \approx 15$  nT over a bandwidth of 12.5 Hz. However, every 5 minutes, the in-loop sensor signal was zeroed, and the NV-NMR machine was recalibrated to avoid slow drifts of the field. This approach effectively erased information about longterm magnetic field drifts, while the microwave retuning described here only cancels temperature drifts to stay on the resonances, and thus conserves the longterm magnetic field information.

#### IV. CONCLUSION

In this article we presented a direct magnetic field stabilization based on NV centers, which is compatible with intermediate magnetic fields at the typical scales in cold atom experiments. Our prototype achieved performances which are better than the state-of-the-art for quantum gas experiments at high magnetic fields. The sensitivity of the sensor can be improved further by utilizing better diamond samples, higher collection and excitation efficiencies, increasing the size of the used ensemble [14, 15, 17], using magnetic flux concentrating materials [18] or microwave cavity readout [40, 41]. A fiber based approach to reading out the NV's spin states [42–44] could allow for an even more compact design, which would open the route to applications in confined spaces. With several magnetic field sensors positioned suitably around the cold atom chamber we could extend the scheme beyond the control of magnetic offset fields and directly control strong magnetic field gradients.

Altogether, this technology could allow for a new class of precision experiments in atomic physics at magnetic field strengths previously not accessible. One route here would be experiments on Feshbach resonances, for instance for the quantum simulation of dipolar droplets [6], where the magnetic field stability would improve by up to two orders of magnitude from  $\sim 1$   $\mu$ T to the demonstrated  $\sigma_{DC} = 12$  nT, or the study of supersolid behaviors at high field values in dipolar quantum gases [45, 46]. Another possible application is the study of spin changing collisions between bosonic and fermionic species. For Bose-Bose mixtures, these resonances typically lie in the range of a hundred  $\mu$ T and have been successfully employed before as a building block of abelian lattice gauge theories [4, 47]. However, for the simulation of quantum electrodynamics it will be necessary to employ fermionic atoms, which emulate the role of the fermionic charges. For the scattering of a bosonic and a fermionic species

they occur at much higher field strengths, e.g. for the case of  $^{23}\text{Na}$  and  $^{40}\text{K}$  in the vicinity of 30 mT. The field stability  $\sigma_{DC}$  results in an energy stability in the order of 100 Hz here, which is putting the quantum simulation of quantum electrodynamics into an accessible regime [7].

Finally, the hybrid of ultracold quantum gases and color centers might allow for a new class of experiments at the interface of these two quantum systems. One possible application here would be the cross validation of the previously measured g-factor of the NV center [48–50] with higher precision than done before.

#### ACKNOWLEDGMENTS

This work is part of and supported by the DFG Collaborative Research Centre “SFB 1225 (ISOQUANT)”. F. J. acknowledges the DFG support through the project FOR 2724, the Emmy-Noether grant (project-id 377616843) and from the Juniorprofessorenprogramm Baden-Württemberg (MWK). D.D. and J.W. acknowledge financial support by the German Science Foundation (DFG) (SPP1601, FOR2724), the EU (ERC) (AS-TERIQS, SMel), the Max Planck Society, the Volkswagen Stiftung. We thank Helmut Strobel for helpful discussions and Leonhard Neuhaus for advice on modifying PyRPL's FPGA. The raw data and the data treatment are accessible online [51].

#### Appendix A: Optical setup

For both sensors used in this work the optical setups are identical, with exception of the laser: Either a Laser Quantum Finesse laser or a 520 nm diode laser acquired off ebay supply approximately 900 mW of excitation light. We focus it down onto the diamond samples using a  $f=200$  mm lens, and collect the fluorescence using a compound parabolic concentrator (Edmund Optics, with a  $25^\circ$  collection angle and a 4.3 mm exit diameter). The fluorescence passes a 650 nm longpass filter (Thorlabs FEL0650) to filter out any remaining excitation light before being focused onto the signal photodiode of an autobalanced photodetector (Nirvana Auto-Balanced Photoreceivers Model 2007).

To collect a reference beam for our photodetector, the excitation beam is sent through a  $\lambda/2$  waveplate as well as a beam sampler (Thorlabs BSF10-A). The sampled beam passes through a diffuser (Thorlabs DG10-220-A) to remove etalon fringing and similar effects before being detected and used as the reference on the autobalanced photodetector.

#### Appendix B: Microwave setup and control loop

In order to keep both the microwave setup and the control loop (illustrated on the left in Fig 6) compact,

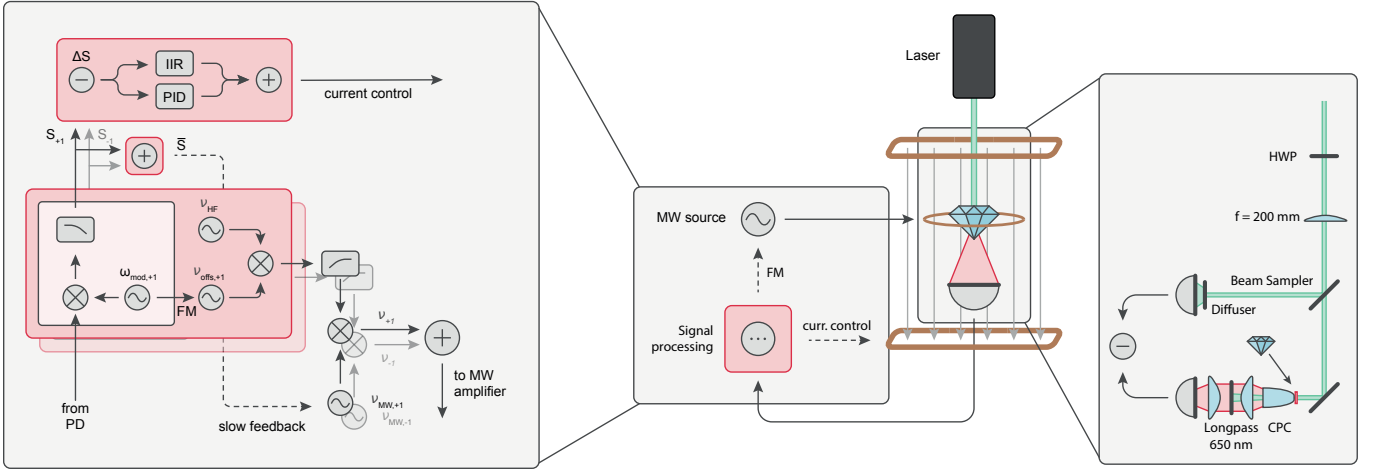


FIG. 6. Overview over the experimental setup, with a breakout for the microwave setup and control loop on the left, and the optical setup on the right. All elements enclosed in a red box are realized on the FPGA of a StemLab RedPitaya, with the lock in amplifier components grouped in a lighter colored box.

much of the functionality was realized on the FPGA of a Red Pitaya STEMLab 125-14 board using a modified version of PyRPL [36]. This allows us to use only few additional components to shift the frequencies into the GHz regime.

To cancel out the temperature noise in our signal, both transitions  $m_s = 0 \rightarrow m_s = -1$  and  $m_s = 0 \rightarrow m_s = +1$  are monitored simultaneously. This is possible by frequency modulating the microwave signals driving the transitions at different frequencies  $\omega_{\text{mod},-1}$  and  $\omega_{\text{mod},+1}$ . The two signals are separated by demodulating the fluorescence at said frequencies using a lock-in scheme.

The frequency modulation is generated on a frequency  $\nu_{\text{offs},-1}$  as well as  $\nu_{\text{offs},+1}$  directly on the RedPitaya's FPGA. Afterwards, the signals are mixed with the NV center's hyperfine splitting  $\nu_{\text{HF}}$  to generate sidebands at  $\approx 2.2$  MHz. These signals are then outputted via the RedPitaya's fast DACs, and high pass filtered afterwards (using Mini-Circuits ZFHP-0R50-S+ high pass filters) to remove any low frequency output (due to technical constraints, the current control signal is outputted on the same DAC). This filtered signal is then mixed (Mini-Circuits ZX05-43H-S+) with the microwave frequencies  $\nu_{\text{MW},-1}$  and  $\nu_{\text{MW},+1}$  (generated by the two channels of a Windfreaktech SynthHD) to shift the frequencies to the GHz regime, creating the frequencies  $\nu_{-1}$  and  $\nu_{+1}$ . Finally, the two signals are added together using a power splitter (Mini-Circuits ZX10-2-442-S+) and fed into an amplifier (a Mini Circuits ZHL-16W-43-S+ in-loop or a Mini-Circuits ZHL-15W-422+ out of loop). The amplifier output is applied to the diamond samples via a wire loop glued to the same sapphire glass heatsink as the sample.

Meanwhile, the output of the two lock-in modules  $S_{-1}$  and  $S_{+1}$  on the RedPitaya is normalized and subtracted (added) together to generate the signals  $\Delta S$  ( $\bar{S}$ ).  $\bar{S}$  is used in the temperature noise cancellation scheme ex-

plained in the next section, while  $\Delta S$  is fed into both a PI controller as well as into an IIR filter programmed to amplify noise at 50 Hz and harmonics to achieve a stronger noise suppression at those frequencies. Both outputs are added together and outputted on one of the RedPitaya's fast DACs. This control signal is then fed into a home built current controller regulating the current through a low inductance coil pair, and thus stabilizing the magnetic field.

### Appendix C: Temperature noise cancellation scheme

Great care has to be taken in order to extract an error signal only containing the magnetic field reading along the axis of interest, and not any off-axis components or temperature fluctuation signals. Conveniently, both off-axis fluctuations as well as temperature fluctuations move the two transitions  $m_s = 0 \rightarrow m_s = -1$  and  $m_s = 0 \rightarrow m_s = 1$  in unison, while the on axis fluctuations move them in opposite directions, as illustrated in Fig. 1 B. This allows to extract the on-axis magnetic field reading by subtracting the normalized error signals generated on both transitions independently. To normalize these signals, magnetic field fluctuations at a frequency with a low noise floor were generated on the feedback coil pair, and their effect on the sum signal  $\bar{S}$  was minimized by scaling the two error signals accordingly.

One issue that can occur in this configuration is that the temperature drifts far enough to shift the transitions away from the two microwave frequencies  $\nu_{-1}$  and  $\nu_{+1}$  - luckily, this can be circumvented by observing the sum signal  $\bar{S}$  and retuning the absolute microwave frequencies (while keeping their relative distance, which sets the magnetic field strength), keeping  $\bar{S}$  near zero.

A crude feedback loop - consisting of several measurements of  $\bar{S}$  followed by a retuning of the microwave fre-



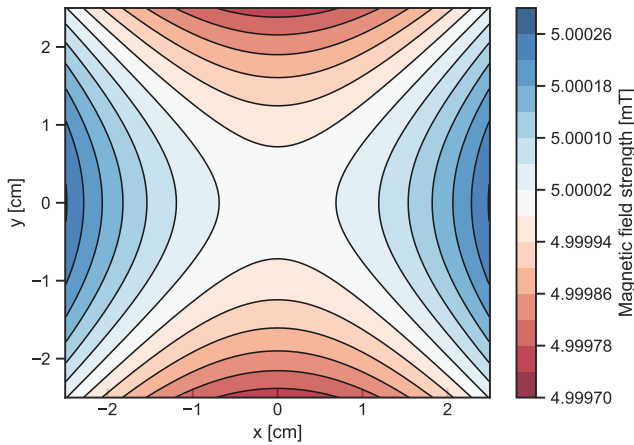


FIG. 7. Magnetic field homogeneity of the Helmholtz coil pair in the  $xy$ -plane with  $z = 0$ . The  $y$ -axis is oriented along the Helmholtz coil axis, and spans the horizontal plane together with the  $x$ -axis.

quencies in order to regulate the sum signal - was implemented for the measurements presented in this work. Even though it generates some noise for every retuning (as can be seen on the peak at 60 s in Fig. 5), it is essential to ensure the long-term functionality of the feedback loop, and to prevent it from falling out of lock.

## Appendix D: Magnetic field generation

We employ a pair of coils of side lengths  $33.5 \text{ cm} \times 28.5 \text{ cm}$  with 80 windings each and separated by  $15.5 \text{ cm}$  to generate our magnetic bias field. A second coil pair with only 16 windings wrapped around the first coil pair is used for regulating the magnetic field over a larger bandwidth. While the bias coil pair is driven by a Delta Elektronika SM 18-50, this coil pair is regulated using a homebuilt current driver.

One requirement for the magnetic field in our application is to be homogeneous over both sensors to ensure that the signals read out are identical. For this, the coil geometry used was simulated using Radia [52], yielding inhomogeneities below 50 ppm for 1 cm total misalignment of the two sensors with respect to the coil pair's center. As the AC magnetic field fluctuations we want to stabilize are on the order of  $1 \mu\text{T}/\sqrt{\text{Hz}}$  and below, this is currently not limiting. However, magnetic field gradients leading to different sensor readings can also be generated by external sources, like 50 Hz power line noise, making it desirable to keep both sensors as close together as possible.

In a similar manner, the magnetic field inside the diamond samples was simulated. As inhomogeneities here lead to a broadening of the resonances for large magnetic fields, the sensitivity  $S$  can be calculated using the magnetic field spread  $\Delta B$  and the system's transition linewidth at zero magnetic field  $\Delta f$ :

$$S \propto \sqrt{\frac{\Delta f}{\sqrt{\Delta f^2 + \Delta B^2} \cdot \gamma_e^2}} \quad (\text{D1})$$

Based on this scaling, we expect the sensitivity of our sensor to decrease by 50 % past a field value of 2.2 T.

- 
- [1] H. Strobel, W. Muessel, D. Linnemann, T. Zibold, D. B. Hume, L. Pezzè, A. Smerzi, and M. K. Oberthaler, *Science* **345**, 424 (2014).
  - [2] W. Muessel, H. Strobel, D. Linnemann, D. B. Hume, and M. K. Oberthaler, *Phys. Rev. Lett.* **113**, 103004 (2014).
  - [3] M. Prüfer, P. Kunkel, H. Strobel, S. Lannig, D. Linnemann, C.-M. Schmied, J. Berges, T. Gasenzer, and M. K. Oberthaler, *Nature* **563**, 217 (2018).
  - [4] A. Mil, T. V. Zache, A. Hegde, A. Xia, R. P. Bhatt, M. K. Oberthaler, P. Hauke, J. Berges, and F. Jendrzejewski, *Science* **367**, 1128 (2020).
  - [5] P. Ripka, *Sensors and Actuators A: Physical* **33**, 129 (1992).
  - [6] C. R. Cabrera, L. Tanzi, J. Sanz, B. Naylor, P. Thomas, P. Cheiney, and L. Tarruell, *Science* **359**, 301 (2018).
  - [7] T. V. Zache, F. Hebenstreit, F. Jendrzejewski, M. K. Oberthaler, J. Berges, and P. Hauke, *Quantum Science and Technology* **3**, 034010 (2018).
  - [8] F. Baudenbacher, L. Fong de los Santos, J. Holzer, and M. Radparvar, *Appl. Phys. Lett.* **82**, 3487 (2003).
  - [9] D. Drung, C. Abmann, J. Beyer, A. Kirste, M. Peters, F. Ruede, and T. Schurig, *IEEE Transactions on Applied Superconductivity* **17**, 699 (2007).
  - [10] H. B. Dang, A. C. Maloof, and M. V. Romalis, *Applied Physics Letters* **97**, 151110 (2010).
  - [11] W. C. Griffith, S. Knappe, and J. Kitching, *Optics Express* **18**, 27167 (2010).
  - [12] V. G. Lucivero, P. Anielski, W. Gawlik, and M. W. Mitchell, *Review of Scientific Instruments* **85**, 113108 (2014).
  - [13] W. Muessel, H. Strobel, D. Linnemann, D. B. Hume, and M. K. Oberthaler, *Phys. Rev. Lett.* **113**, 103004 (2014).
  - [14] T. Wolf, P. Neumann, K. Nakamura, H. Sumiya, T. Ohshima, J. Isoya, and J. Wrachtrup, *Phys. Rev. X* **5**, 041001 (2015).
  - [15] J. F. Barry, M. J. Turner, J. M. Schloss, D. R. Glenn, Y. Song, M. D. Lukin, H. Park, and R. L. Walsworth, *Proceedings of the National Academy of Sciences* **113**, 14133 (2016).
  - [16] J. M. Schloss, J. F. Barry, M. J. Turner, and R. L.

- Walsworth, Phys. Rev. Applied **10**, 034044 (2018).
- [17] H. Clevenson, M. E. Trusheim, C. Teale, T. Schröder, D. Braje, and D. Englund, Nature Physics **11**, 393 (2015).
  - [18] I. Fescenko, A. Jarmola, I. Savukov, P. Kehayias, J. Smits, J. Damron, N. Ristoff, N. Mosavian, and V. M. Acosta, Physical Review Research **2**, 23394 (2020).
  - [19] D. R. Glenn, D. B. Bucher, J. Lee, M. D. Lukin, H. Park, and R. L. Walsworth, Nature **555**, 351 (2018).
  - [20] J. C. Jaskula, K. Saha, A. Ajoy, D. J. Twitchen, M. Markham, and P. Cappellaro, Physical Review Applied **11**, 1 (2019).
  - [21] S. Steinert, F. Dolde, P. Neumann, A. Aird, B. Naydenov, G. Balasubramanian, F. Jelezko, and J. Wrachtrup, Review of Scientific Instruments **81**, 043705 (2010).
  - [22] *A1304 Linear Hall-Effect Sensor IC with Analog Output, Available in a Miniature, Low-Profile Surface Mount Package*, Allegro microsystems (2019), rev. 3.
  - [23] *A1324, A1325, and A1326 Low-Noise Linear Hall-Effect Sensor ICs with Analog Output*, Allegro microsystems (2020), rev. 8.
  - [24] E. Ramsden, *Hall-Effect Sensors*, 2nd ed. (Newnes, 2011) theory and Application.
  - [25] A. Grosz, M. J. Haji-Sheikh, and S. C. Mukhopadhyay, *High Sensitivity Magnetometers*, Vol. 19 (Springer, 2017).
  - [26] B. Dufay, S. Saez, C. Dolabdjian, A. Yelon, and D. Menard, IEEE Transactions on Magnetics **49**, 85 (2013).
  - [27] J. R. Kirtley, M. B. Ketchen, K. G. Stawiasz, J. Z. Sun, W. J. Gallagher, S. H. Blanton, and S. J. Wind, Applied Physics Letters **66**, 1138 (1995).
  - [28] A. Finkler, Y. Segev, Y. Myasoedov, M. L. Rappaport, L. Ne'Eman, D. Vasyukov, E. Zeldov, M. E. Huber, J. Martin, and A. Yacoby, Nano Letters **10**, 1046 (2010).
  - [29] R. Nagendran, N. Thirumurugan, N. Chinnasamy, M. P. Janawadkar, and C. S. Sundar, Review of Scientific Instruments **82**, 015109 (2011).
  - [30] V. Stepanov, F. H. Cho, C. Abeywardana, and S. Takahashi, Applied Physics Letters **106**, 063111 (2015).
  - [31] J. Wrachtrup, C. von Borczyskowski, J. Bernard, M. Orrit, and R. Brown, Nature **363**, 244 (1993).
  - [32] V. Ivády, T. Simon, J. R. Maze, I. A. Abrikosov, and A. Gali, Phys. Rev. B **90**, 235205 (2014).
  - [33] W. Welford and R. Winston, *The Optics of Nonimaging Concentrators: Light and Solar Energy* (Academic Press, New York, 1978).
  - [34] P. C. D. Hobbs, "Noise cancelling circuitry for optical systems with signal dividing and combining means," (1992), US Patent 5,134,276.
  - [35] P. C. D. Hobbs, *Building Electro-Optical Systems: Making it all work* (John Wiley & Sons, Ltd, 2008).
  - [36] L. Neuhaus, R. Metzдорff, S. Chua, T. Jacqmin, T. Briant, A. Heidmann, P. . Cohadon, and S. Deléglise, in *2017 Conference on Lasers and Electro-Optics Europe European Quantum Electronics Conference (CLEO/Europe-EQEC)* (2017) pp. 1–1.
  - [37] J. Vijayan, P. Sompet, G. Salomon, J. Koepsell, S. Hirthe, A. Bohrdt, F. Grusdt, I. Bloch, and C. Gross, Science **367**, 186 (2020).
  - [38] T. Schweigler, V. Kasper, S. Erne, I. Mazets, B. Rauer, F. Cataldini, T. Langen, T. Gasenzer, J. Berges, and J. Schmiedmayer, Nature **545**, 323 (2017).
  - [39] H. Clevenson, L. M. Pham, C. Teale, K. Johnson, D. Englund, and D. Braje, Applied Physics Letters **112**, 252406 (2018).
  - [40] E. R. Eisenach, J. F. Barry, M. F. O'Keeffe, J. M. Schloss, M. H. Steinecker, D. R. Englund, and D. A. Braje, (2020), 2003.01104.
  - [41] J. Ebel, T. Joas, M. Schalk, A. Angerer, J. Majer, and F. Reinhard, (2020).
  - [42] S. M. Blakley, I. V. Fedotov, S. Y. Kilin, and A. M. Zheltikov, Opt. Lett. **40**, 3727 (2015).
  - [43] I. V. Fedotov, L. V. Doronina-Amitonova, D. A. Sidorov-Biryukov, N. A. Safronov, S. Blakley, A. O. Levchenko, S. A. Zibrov, A. B. Fedotov, S. Y. Kilin, M. O. Scully, V. L. Velichansky, and A. M. Zheltikov, Opt. Lett. **39**, 6954 (2014).
  - [44] I. V. Fedotov, L. V. Doronina-Amitonova, A. A. Voronin, A. O. Levchenko, S. A. Zibrov, D. A. Sidorov-Biryukov, A. B. Fedotov, V. L. Velichansky, and A. M. Zheltikov, Scientific Reports **4**, 5362 (2014).
  - [45] L. Chomaz, D. Petter, P. Ilzhöfer, G. Natale, A. Trautmann, C. Politi, G. Durastante, R. M. W. van Bijnen, A. Patscheider, M. Sohmen, M. J. Mark, and F. Ferlaino, Phys. Rev. X **9**, 021012 (2019).
  - [46] F. Böttcher, J.-N. Schmidt, M. Wenzel, J. Hertkorn, M. Guo, T. Langen, and T. Pfau, Phys. Rev. X **9**, 011051 (2019).
  - [47] X. Li, B. Zhu, X. He, F. Wang, M. Guo, Z.-F. Xu, S. Zhang, and D. Wang, Phys. Rev. Lett. **114**, 255301 (2015).
  - [48] J. H. Loubser and J. A. Van Wyk, Reports on Progress in Physics **41**, 1201 (1978).
  - [49] M. W. Doherty, N. B. Manson, P. Delaney, and L. C. Hollenberg, New Journal of Physics **13**, 025019 (2011).
  - [50] I. V. Zhukov, S. V. Anishchik, and Y. N. Molin, Applied Magnetic Resonance **48**, 1461 (2017).
  - [51] A. Hesse, K. Köster, J. Steiner, J. Michl, V. Vorobyov, D. Dasari, J. Wrachtrup, and F. Jendrzejewski, "Direct control of high magnetic fields for cold atom experiments based on NV centers [Dataset]," (2020).
  - [52] O. Chubar, P. Elleaume, and J. Chavanne, Journal of Synchrotron Radiation **5**, 481 (1998).